Journal of Advanced Ceramics
先进陶瓷
ISSN 2226-4108
CN 10-1154/TQ
清华大学出版社 Tsinghua University Press
SciOpen

J Adv Ceram 2026, **15**: 9221367

https://doi.org/10.26599/JAC.2026.9221367

Research Article

Low-temperature densification of constrained GDC interlayers via chemo-mechanical regulation for stable solid oxide fuel cells

Fuhuan Wang[1, †], Yuechao Yao[1, †], Yucan Liu[2,3, †], Weifeng Zhang[1], Yanmin Wang[1], Xiaojie Cheng[1], Jun Zhang[1,*], Yucun Zhou[1,*], Liangfei Xu[1,2,3], Shaorong Wang[1,4], Hewu Wang[2,3], Jianqiu Li[1,2,3,*]

[1] *Beijing Huairou Laboratory, Beijing 101400, China.*

[2] *State Key Laboratory of Intelligent Green Vehicle and Mobility, Tsinghua University, Beijing 100084, China.*

[3] *School of Vehicle and Mobility, Tsinghua University, Beijing 100084, China.*

[4] *School of Chemistry and Chemical Engineering, China University of Mining and Technology, Xuzhou 221116, China.*

[†] These authors contributed equally to this work.

* Corresponding author.

E-mail: J. Zhang, zhangjun@hrl.ac.cn;

Y. Zhou, zhouyucun@hrl.ac.cn;

J. Li, lijianqiu@tsinghua.edu.cn

Received: July 2, 2026; Revised: August 18, 2026; Accepted: August 28, 2026

Abstract: Constrained densification of ceramic interlayers in solid oxide fuel cells (SOFCs) is strongly influenced by the interplay between constraint effects and diffusion kinetics. While elevated sintering temperatures are commonly employed to overcome stress-retarded densification, they simultaneously accelerate interfacial interdiffusion and reaction-layer formation, creating a long-standing trade-off between microstructural integrity and chemical stability. Here, we demonstrate a chemo-mechanical regulation strategy that effectively mitigates the conflict between these competing processes through concurrent enhancement of sintering kinetics and regulation of green-state packing homogeneity. By combining Co_3O_4-assisted sintering activation with cold isostatic pressing (CIP), ultrathin Gd-doped ceria (GDC) interlayers achieve an apparent relative density of 98.5% after constrained sintering, enabling densification at 1200 °C, below the temperatures commonly reported for constrained GDC films processed without sintering activation. The resulting dense and continuous interlayer limits Ce–Zr interdiffusion during fabrication and mitigates Sr-related interfacial reaction and reaction-layer formation during operation. Consequently, the optimized anode-supported SOFC delivers a peak power density of 1.36 $W \cdot cm^{-2}$ at 800 °C and exhibits a normalized degradation rate of 0.48% per 1000 h, calculated from the stabilized 200–460 h operation period at 750 °C. Accelerated thermal aging at 850 °C for 600 h further supports the stability of the engineered heterointerface. The chemo-mechanical strategy was successfully extended to 10 × 10 cm^2 cells, supporting its compatibility with scalable wet-processing routes. This work provides a chemo-mechanical perspective for mitigating the interplay between constrained densification and interfacial reactivity in multilayer ceramic systems.

Keywords: Solid oxide fuel cells; Gadolinium-doped ceria interlayer; Constrained sintering; Chemo-mechanical regulation; Interface stability; Scalable manufacturing.

1 Introduction

Solid oxide fuel cells (SOFCs) are among the most efficient electrochemical energy-conversion technologies for sustainable power generation owing to their fuel flexibility, high electrical efficiency, low emissions, and all-solid-state architecture [1–3]. Recent advances in electrode and electrolyte materials have enabled progressive reduction of operating temperatures toward the intermediate-temperature regime of 650–800 °C, thereby mitigating thermal degradation and lowering system costs [4]. Nevertheless, long-term durability remains a major barrier to widespread commercialization.

Among the degradation processes operating in intermediate-temperature SOFCs, chemical instability at the cathode/electrolyte interface is particularly detrimental because it directly affects oxygen-ion transport and electrochemical reaction kinetics [5,6]. $La_{0.6}Sr_{0.4}Co_{0.2}Fe_{0.8}O_{3-\delta}$ (LSCF) is widely regarded as one of the most promising cathode materials owing to its excellent oxygen-reduction activity and mixed ionic–electronic conductivity (MIEC) [6,7]. However, thermally activated Sr segregation continuously enriches the cathode/electrolyte interface during fabrication and operation [8]. The segregated Sr species readily react with yttria-stabilized zirconia (YSZ) electrolytes to form insulating $SrZrO_3$ phases, while concomitant cation interdiffusion may further generate poorly conductive reaction regions that progressively increase polarization resistance and accelerate performance degradation [6,9,10]. Extensive durability studies have demonstrated that interfacial chemical evolution rather than intrinsic bulk transport frequently becomes one of the dominant lifetime-limiting factors in advanced SOFC systems [11,12].

To mitigate these degradation pathways, gadolinium-doped ceria (GDC) interlayers have been widely introduced between LSCF cathodes and YSZ electrolytes [5,6]. Owing to their high oxygen-ion conductivity and favorable chemical compatibility with both adjacent components, dense GDC barriers can effectively suppress Sr migration, reduce interfacial reaction kinetics, and preserve continuous ionic-transport pathways across the heterointerface [8,13]. Considerable effort has therefore been devoted to fabricating thin and highly dense ceria-based interlayers capable of

simultaneously limiting transport resistance and optimizing chemical stability [13,14]. Functional interlayers prepared by pulsed laser deposition, sputtering, and atomic layer deposition have demonstrated effectiveness in suppressing interfacial degradation and enhancing durability [15–17]. However, the reliance on sophisticated vacuum-processing techniques limits throughput, manufacturing area, and industrial scalability [16].

In contrast, wet-processing routes including screen printing, spin coating, spray coating, and inkjet printing offer direct compatibility with established ceramic manufacturing infrastructure and are therefore more attractive for practical SOFC production [18–21]. The principal challenge is that thin ceramic films experience constrained sintering when attached to rigid substrates [22,23]. Unlike free sintering, in-plane shrinkage is restricted by the substrate, generating tensile stresses that retard densification, inhibit pore elimination, and reduce grain-boundary transport rates [22,24,25]. Wet-processed GDC interlayers generally require elevated sintering temperatures exceeding 1300 °C to achieve sufficient densification under constrained conditions [26]. Unfortunately, the high temperature required for densification accelerates cation interdiffusion, which in turn forms a Ce–Zr solid-solution interdiffusion zone at the interfaces [10,19]. This makes it difficult to achieve both high density and good chemical stability [19].

Constrained sintering theory suggests that densification is strongly influenced by the interaction between constraint-induced stress development and diffusion kinetics rather than thermal activation alone [23,25]. Tensile stresses generated during constrained shrinkage alter local chemical potentials, modify diffusion pathways, and influence pore evolution throughout the sintering process [22,24]. Increasing evidence from ceramic films, multilayer energy devices, and phase-field sintering simulations indicates that stress-dependent microstructural evolution can significantly affect densification trajectories, defect evolution, and long-term interfacial reliability [25,27]. These findings imply that the long-standing densification–stability trade-off in SOFC interlayers may be closely associated with a common stress-influenced diffusion framework. However, despite extensive

investigations of SOFC degradation chemistry, the role of stress-influenced diffusion behavior in governing constrained densification and subsequent interfacial stability remains largely unexplored.

Several approaches have been proposed to lower the densification temperature of ceria-based ceramics. Transition-metal oxide additives can accelerate grain-boundary diffusion and enhance sintering kinetics by promoting defect transport and interfacial mass diffusion [28,29]. Mechanical compaction techniques including cold isostatic pressing (CIP) improve apparent green density and particle-packing homogeneity, thereby reducing pore connectivity prior to sintering [30,31]. These two approaches therefore address different stages of constrained sintering. Kinetic activation primarily promotes mass transport during firing [19,28], whereas mechanical compaction modifies the initial packing state before firing [31]. Whether combining the two can effectively overcome the densification limitation of constrained GDC films remains insufficiently explored.

We hypothesize that constrained densification and subsequent interfacial evolution may be coupled through stress-influenced diffusion processes. Unlike our previous spin-coating approach [21], which primarily relied on chemical sintering activation, the present work introduces mechanical packing regulation through cold isostatic pressing (CIP) and separately examines the roles of kinetic activation and green-state packing under constrained sintering. Here, chemo-mechanical regulation refers to the combined use of Co_3O_4-assisted sintering to enhance mass transport during firing and CIP to improve green-state packing. This combined strategy is designed to address both the transport kinetics and initial pore/packing state that govern constrained densification. We therefore investigate whether this approach enables compact GDC film at 1200 °C while maintaining compatibility with scalable wet-processing routes.

2 Experimental Section

2.1 Fabrication of Anode-Supported Half-Cells

Anode-supported half-cells were fabricated by a tape-casting and screen-printing route. NiO powder (A Grade, Seido) and 8YSZ powder (TZ-8Y, Tosoh) were used for substrate and electrolyte fabrication.

NiO–YSZ support substrates (60:40 wt.%) were prepared from ethanol-based slurries containing pore former, dispersant, and binder. Green tapes (~600 μm) were laminated at 20 MPa and pre-sintered at 1100 °C for 2 h in air. An anode functional layer (NiO:YSZ = 55:45 wt.%, ~10 μm) and a dense YSZ electrolyte layer (~10 μm) were subsequently screen printed, and the assemblies were co-sintered at 1375 °C for 5 h, yielding dense YSZ electrolytes (~10 μm) supported on porous Ni–YSZ substrates (~500 μm). The resulting 10 × 10 cm^2 half-cells were used for both large-area cell fabrication and button-cell testing. For button-cell evaluation, circular pieces with a diameter of 12 mm were laser-cut from the 10 × 10 cm^2 half-cells.

2.2 Preparation of Constrained GDC Interlayers

Commercial $Ce_{0.8}Gd_{0.2}O_{2-\delta}$ (GDC20, Terio Corporation) powder was dispersed in ethanol (99.7%, Greagent) at a solid loading of 35 wt.% using polyvinyl butyral (PVB, Mw≈40,000–70,000, Aladdin) as binder. Co_3O_4 nanoparticles (99.0%, Aladdin) were added at 2 wt.% relative to GDC as a sintering aid. The selection of transition-metal oxide additives was motivated by previous studies demonstrating enhanced mass transport and stress relaxation in constrained GDC films containing sintering activators [21,29].

The suspension was homogenized using planetary mixing and subsequently deposited onto YSZ electrolyte surfaces by spin coating at 3000 rpm for 30 s. To decouple the individual contributions of chemical activation and mechanical densification, four processing routes were investigated: (i) pristine GDC; (ii) Co_3O_4-assisted GDC; (iii) CIP-treated pristine GDC; (iv) chemo-mechanically processed GDC (Co_3O_4 + CIP). CIP was conducted after coating by vacuum-sealing the half-cells and applying an isostatic pressure of 400 MPa for 5 min. The CIP treatment was intended to homogenize particle packing, reduce pore connectivity, and modify the pore structure and the effective constraint conditions during subsequent constrained sintering [22,30,31]. All interlayers were sintered at 1200 °C for 3 h in air.

Relative green densities were calculated after binder burnout at 500 °C using the measured coating mass, film thickness, and deposition area, taking the theoretical density of GDC20 (7.22 $g \cdot cm^{-3}$) as the reference value [32].

2.3 Cathode Fabrication and Cell Assembly

For button-cell testing, LSCF ($La_{0.6}Sr_{0.4}Co_{0.2}Fe_{0.8}O_{3-\delta}$) cathode powder was synthesized by co-precipitation method according to a previously reported procedure [33]. The obtained powder was formulated into an ink and screen printed directly onto the GDC interlayers, followed by calcination at 1050 °C for 2 h in air. Porous cathode layers with a thickness of ~20 μm were obtained. Button cells possessed an active area of 0.28 cm^2.

To evaluate scalability, large-area cells (10 × 10 cm^2, active area = 81 cm^2) were fabricated using LSCF–GDC composite cathodes (60:40 wt.%) to alleviate thermomechanical mismatch during large-area operation and thermal cycling [34].

2.4 Electrochemical Characterization

Prior to testing, NiO-containing anodes were reduced in flowing H_2 at 800 °C for 2 h. Current density–voltage (I–V) and power density measurements were performed between 650 and 800 °C using humidified H_2 (25 $mL \cdot min^{-1}$) as fuel and ambient air as oxidant. Electrochemical impedance spectroscopy (EIS) measurements were conducted using a Gamry Interface 1000 electrochemical workstation (Gamry Instruments, USA) under open-circuit voltage (OCV) conditions over a frequency range from 10^5 to 10^{-1} Hz using a perturbation amplitude of 10 mV [35].

To elucidate electrochemical losses, the EIS spectra were analyzed using equivalent-circuit fitting and distribution of relaxation times (DRT) analysis [36]. The spectra were fitted using an L–R_Ω–(R1//CPE1)–(R2//CPE2) equivalent circuit. Here, L represents the parasitic inductive contribution, while R_Ω represents the total ohmic resistance. The two R//CPE sub-circuits were used to reproduce the dominant polarization response. Because individual equivalent-circuit elements do not have a unique correspondence to elementary reactions, they are not assigned to specific microscopic processes.

The extracted ohmic resistance (R_Ω), polarization resistance (R_p), and area-specific resistance (ASR) values are summarized in Table S2.

Long-term galvanostatic durability testing was performed at 750 °C under a constant current density of 0.25 $A \cdot cm^{-2}$ for 460 h. To evaluate interfacial stability, symmetric cells with the configuration LSCF–GDC/GDC/YSZ/GDC/LSCF–GDC used a ~200 μm YSZ electrolyte, ~1.8 μm dense GDC interlayers, ~20 μm porous composite cathodes, an electrode porosity of ~35 vol.%, and an active area of 0.28 cm^2. These symmetric cells were subjected to accelerated aging in air at 850 °C for 600 h with periodic impedance monitoring.

For large-area cells, hydrogen was supplied at 600 $mL \cdot min^{-1}$ while air was supplied at a flow rate corresponding to an H_2/air volumetric ratio of 1:5.

2.5 Structural Characterization

Phase compositions were analyzed by X-ray diffraction (XRD, D8 Advance, Bruker) using Cu Kα radiation. Cross-sectional microstructures and elemental distributions were examined using field-emission scanning electron microscopy (SEM, JEOL JSM-7900F) equipped with energy-dispersive X-ray spectroscopy (EDS). Particle-size distributions were measured by laser diffraction following ultrasonic dispersion in ethanol, and specific surface areas were determined by N_2 adsorption using the Brunauer–Emmett–Teller (BET) method.

To evaluate the influence of chemo-mechanical regulation on constrained densification, relative densities of sintered GDC interlayers were quantified from SEM cross-sections using ImageJ-based image analysis. Three representative regions from each sample were analyzed to estimate the image-derived porosity and apparent relative density. Particular attention was paid to correlating green-state packing homogeneity, constrained densification behavior, and interfacial microstructural evolution.

3 Results and Discussion

3.1 Chemo-Mechanical Regulation of Constrained GDC Films

To decouple the long-standing trade-off between constrained densification and interfacial stability, a chemo-mechanical regulation strategy was implemented. This approach integrates Co_3O_4-assisted kinetic activation with CIP-enabled packing homogenization to cooperatively modify mass transport and pore evolution during the constrained sintering of thin GDC films. As listed in Table S1, the as-received GDC20 powder exhibited a single fluorite phase together with a specific surface area of 10.35 $m^2 \cdot g^{-1}$ and a median particle size (D50) of 153 nm. Such fine particles provide a high thermodynamic driving force for sintering and are therefore suitable for investigating constrained densification behavior. Figure 1a schematically illustrates a proposed stress-influenced diffusion framework that may contribute to the observed densification behavior. In this framework, Co_3O_4 is interpreted primarily as a sintering aid that facilitates mass transport during constrained sintering, whereas CIP modifies particle-packing homogeneity and initial pore structure. The simultaneous regulation of these two factors is expected to influence the constrained densification trajectory of the thin GDC film.

Without chemical or mechanical modification, the pristine GDC interlayer remained highly porous after sintering at 1200 °C, exhibiting an apparent relative density of 80.4% and a thickness of 5.2 μm (Figure 1b,f). The interconnected pore network suggests that the available mass transport was insufficient to overcome the densification retardation imposed by substrate constraint. Incorporating Co_3O_4 increased the apparent relative density to 87.7% and reduced the film thickness to 3.7 μm (Figure 1c,g). This enhancement is attributable to the cobalt-containing additives, which enhance grain-boundary diffusion and neck growth. However, localized residual porosity remained evident, suggesting that kinetic activation alone cannot fully eliminate pore retention arising from heterogeneous particle packing in constrained films. Introducing CIP treatment alone yielded a more homogeneous microstructure with an apparent relative density of 92.6% and a thickness of 3.2 μm (Figure 1d,h). Mechanical compaction increased the relative density after binder burnout from approximately 45.6% to 63.2% (Figure S1–S5), thereby reducing pore connectivity and shortening the initial characteristic diffusion distance. Although the green density continued to increase with CIP

pressure, the incremental gain became small above 400 MPa. Increasing the pressure from 400 to 450 MPa increased the green density by only 0.4 percentage points. Therefore, 400 MPa was selected as a practical processing condition. Nevertheless, isolated closed pores were still retained after sintering due to the limited intrinsic transport kinetics of pure GDC at 1200 °C. The combined treatment triggered near-complete densification, reaching an apparent relative density of 98.5% and a final thickness of only 1.8 μm (Figure 1e,i), leaving only isolated nanoscale pores across the film cross-section.

This synergistic behavior is consistent with a kinetic–geometric coupling framework. Green-density measurements (Figure S6) confirm that higher compaction pressure reduces the initial pore volume before thermal treatment. Geometrically, this reduced pore connectivity shortens the effective diffusion distance for pore elimination during subsequent sintering. It may also alter the local shrinkage behavior of the constrained film. Simultaneously, Co_3O_4-assisted activation is expected to facilitate mass transport during subsequent sintering. This synergistic effect facilitates pore elimination despite the constraint-induced retardation of densification. Although direct stress measurements were not performed in the present study, the observed microstructural evolution is consistent with chemo-mechanical regulation modifying the effective interaction between constrained shrinkage and diffusional transport.

Regarding the cobalt additive, prior studies indicate that Co can modify GDC grain-boundary transport through changes in grain-boundary structure and defect chemistry [37–39]. In the present study, SEM-EDS cannot resolve the atomic-scale distribution or chemical state of Co. We therefore interpret Co_3O_4 primarily as a sintering aid that promotes mass transport during constrained sintering, without assigning a specific atomic-scale Co configuration.

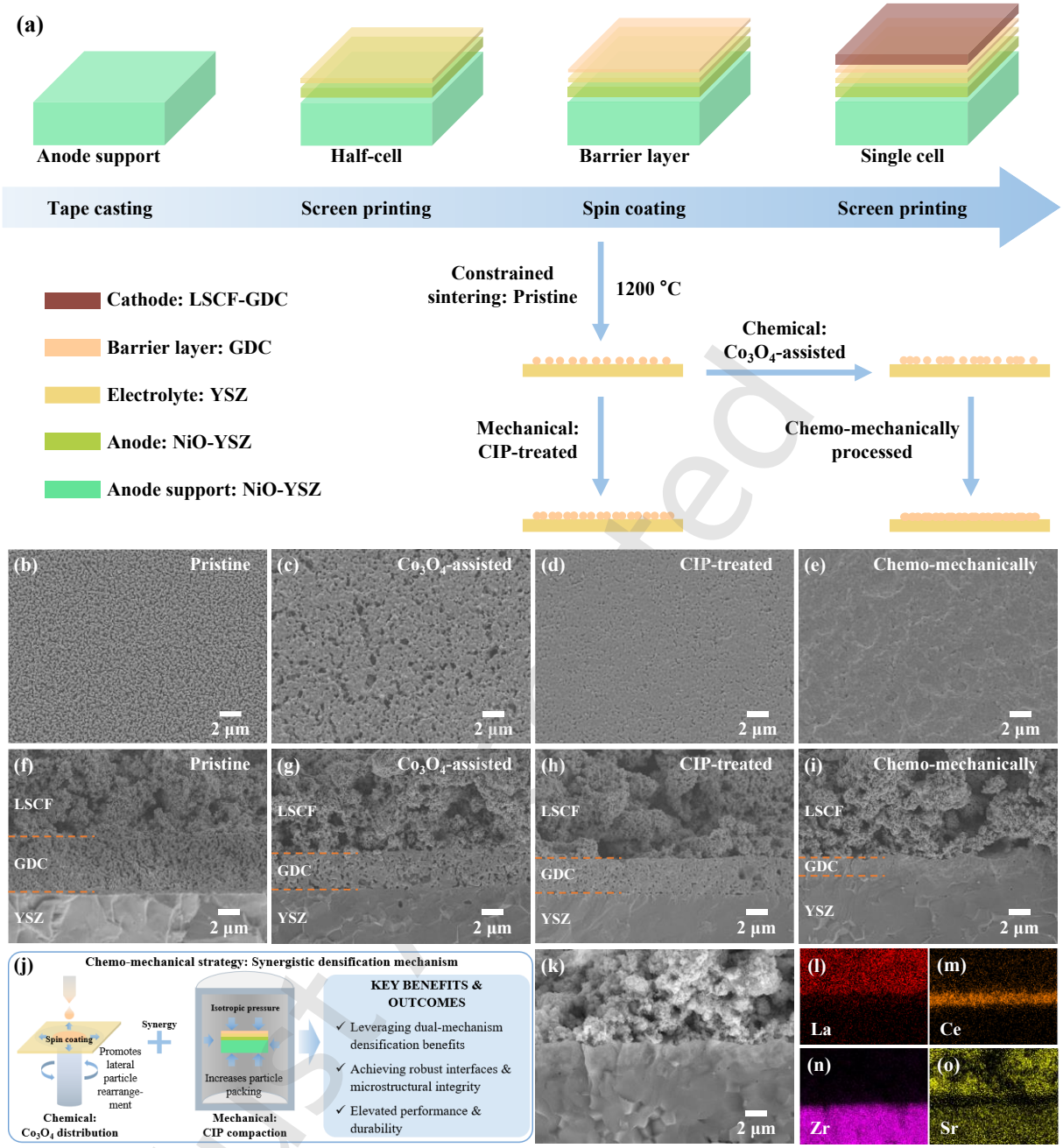

Figure 1 Chemo-mechanical regulation of constrained GDC densification. (a) Schematic illustration of the coupled kinetic-activation and mechanical-compaction strategy for regulating constrained sintering of ultrathin GDC interlayers. Cross-sectional SEM images of GDC films processed by (b,f) pristine sintering, (c,g) Co_3O_4-assisted activation, (d,h) CIP-assisted compaction, and (e,i) combined chemo-mechanical regulation. (j) Schematic illustration of the chemo-mechanical regulation strategy and its advantages. (k–o) Cross-sectional SEM image and corresponding EDS elemental mappings of the chemo-mechanically densified GDC/YSZ heterointerface, showing suppressed interfacial interdiffusion after sintering at 1200 °C.

The influence of this strategy extends directly to the interfacial chemical stability of the heterostructure. Cross-sectional SEM images and corresponding EDS elemental mappings (Figure 1k–o) revealed a dense, continuous, and compositionally intact GDC interlayer with no significant Ce–Zr interdiffusion detectable by SEM-EDS across the GDC/YSZ interface. Because conventional processing above 1250–1300 °C typically triggers the formation of poorly conducting mixed fluorite-type $(Ce,Zr)O_2$ solid solutions [19,37], these results demonstrate that lowering the densification temperature via chemo-mechanical regulation substantially alleviates the long-standing trade-off between constrained densification and interfacial chemical integrity.

3.2 Interfacial Ionic Transport Properties

The influence of chemo-mechanical regulation on electrochemical transport was evaluated by I–V, I–P, EIS, and DRT measurements from 650 to 800 °C. As shown in Figure 2a–d, the cell performance increased with temperature. At 800 °C, the chemo-mechanically processed cell reached a peak power density of 1.36 $W \cdot cm^{-2}$, compared with 1.29, 1.26, and 1.16 $W \cdot cm^{-2}$ for the pristine, Co_3O_4-assisted, and CIP-treated interlayers, respectively. At 750 °C and 0.8 V, the optimized cell achieved a power density of 0.89 $W \cdot cm^{-2}$, which is 17.1%, 11.3%, and 18.7% higher than the pristine (0.76 $W \cdot cm^{-2}$), Co_3O_4-assisted (0.80 $W \cdot cm^{-2}$), and CIP-treated (0.75 $W \cdot cm^{-2}$) cells, respectively.

EIS results provide further insight into the effect of the interlayer processing strategy (Figure 2e–h and Table S2). Both R_Ω and R_p decreased with increasing temperature for all samples. The chemo-mechanically processed cell showed substantially lower ASR than the pristine cell from 650 to 750 °C, with ASR values decreasing from 1.367 to 0.708 $\Omega \cdot cm^2$. At 750 °C, its R_Ω and R_p were 0.070 and 0.638 $\Omega \cdot cm^2$, respectively. At 800 °C, the ASR further decreased to 0.549 $\Omega \cdot cm^2$, remaining comparable to the pristine cell (0.541 $\Omega \cdot cm^2$) and lower than those of the Co_3O_4-assisted (0.589 $\Omega \cdot cm^2$) and CIP-assisted (0.572 $\Omega \cdot cm^2$) cells. These results demonstrate that the chemo-mechanical strategy effectively reduces the overall electrochemical resistance over a broad temperature range. Importantly, the EIS-derived resistances should not be directly equated with voltage losses under high-current

operation. The EIS spectra were recorded at OCV with a 10 mV AC perturbation and characterize the local small-signal response near equilibrium, whereas peak power density was obtained from DC I–V measurements under finite-current conditions, where nonlinear polarization and mass-transport losses also contribute. Therefore, a lower ASR does not necessarily translate directly into a higher peak power density.

The CIP-treated GDC layer reached an apparent relative density of 92.6%, but its peak power density at 800 °C was only 1.16 $W \cdot cm^{-2}$, compared with 1.36 $W \cdot cm^{-2}$ for the chemo-mechanically processed cell. CIP mainly improves the initial particle packing and green-state density, whereas Co_3O_4-assisted sintering is expected to facilitate mass transport during subsequent constrained densification [37,38]. Their combination may lead to a more favorable grain structure, pore distribution, and GDC/YSZ interfacial continuity than either treatment alone, which may become particularly important under finite-current operation.

The Co_3O_4-assisted sintering alone yielded a peak power density of 1.26 $W \cdot cm^{-2}$ at 800 °C, slightly lower than the pristine cell (1.29 $W \cdot cm^{-2}$), indicating that kinetic activation alone was insufficient to improve the electrochemical performance under the present processing conditions. Without CIP, the initial particle packing was less controlled, which may have limited the benefit of the modified sintering behavior. In contrast, combining CIP with Co_3O_4-assisted sintering increased the apparent relative density to 98.5% and gave the highest peak power density of 1.36 $W \cdot cm^{-2}$. The lower power density of the CIP-treated cell, despite its relatively high density of 92.6%, indicates that increasing green density or final density alone does not guarantee improved high-current performance.

The role of Co_3O_4 in the enhanced sintering behavior should also be considered with caution. Cobalt-containing additives can modify GDC sintering and grain-boundary transport through changes in grain-boundary structure and defect chemistry [37–39]. However, the present characterization does not establish whether Co remains at grain boundaries, enters the GDC lattice, or forms a secondary phase after sintering. In particular, the SEM-EDS analysis cannot resolve the atomic-scale distribution

or chemical state of Co, and no Co-rich secondary phase was resolved by SEM-EDS at the spatial resolution and detection limit of the present analysis. We therefore interpret Co_3O_4 here as a sintering aid that promotes mass transport during constrained densification, without assigning a specific atomic-scale configuration to Co. A more definitive description of the Co-containing species would require dedicated structural and chemical-state analyses.

The present results also do not allow the individual contributions of initial particle packing, Co_3O_4-assisted sintering, grain-boundary transport, and interfacial structure to be quantitatively separated. The higher performance of the chemo-mechanically processed cell is therefore attributed to the complementary effects of CIP and Co_3O_4-assisted sintering rather than to the higher density alone. Since the electrode compositions, electrolyte thicknesses, and testing conditions were kept consistent among the cells, the observed performance differences are consistent with differences in the microstructural and interfacial characteristics of the GDC layers, although their individual contributions cannot be separated from the present measurements.

By enabling effective constrained densification at 1200 °C, the combined strategy also avoids the higher-temperature conditions that can promote Ce–Zr interdiffusion while producing a highly densified GDC layer. The resulting heterointerface maintains favorable electrochemical transport without a significant increase in interfacial resistance, highlighting the benefit of combining particle-packing control with Co_3O_4-assisted sintering for low-temperature fabrication of dense GDC interlayers.

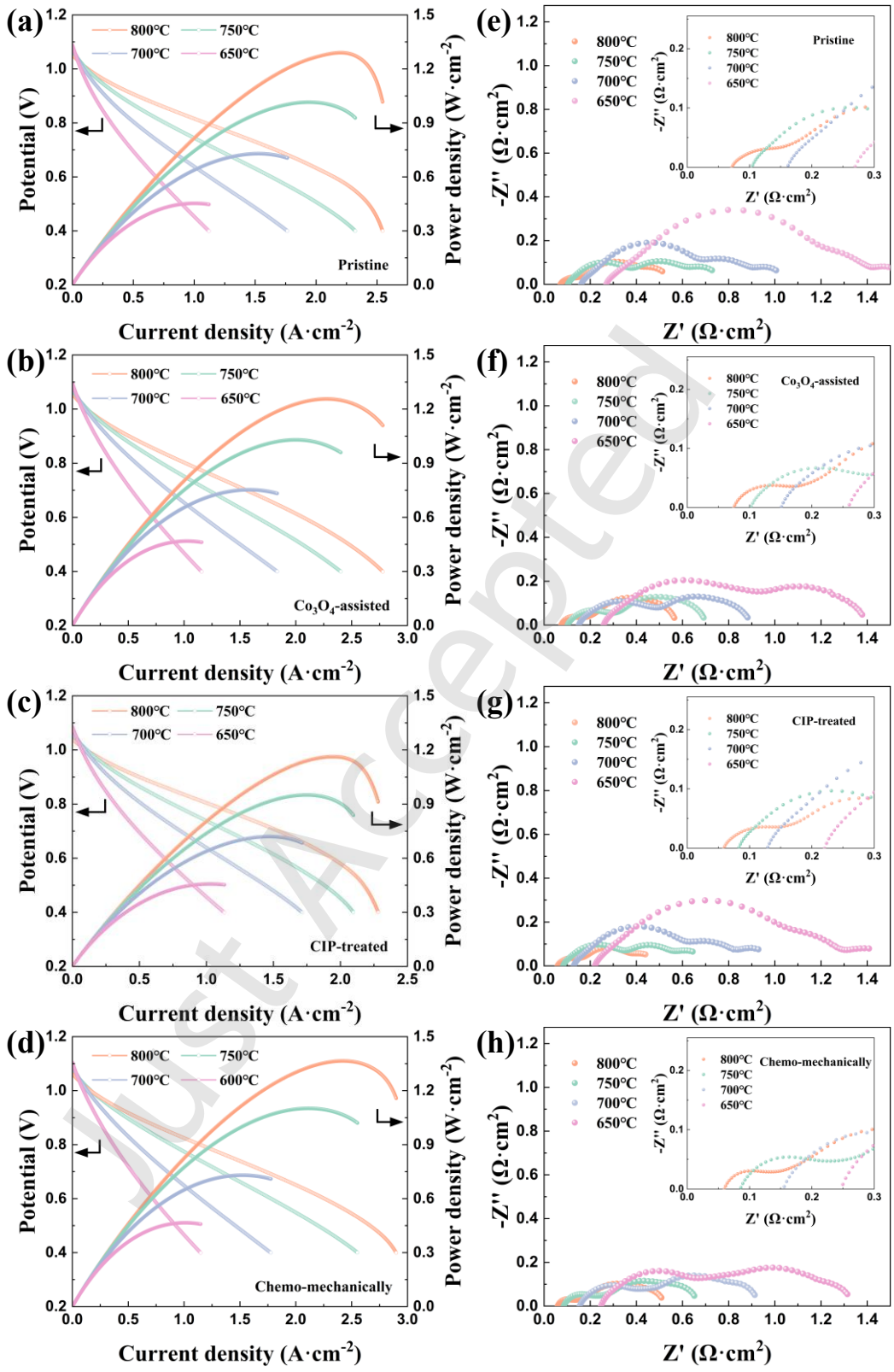

Figure 2 Electrochemical transport behavior of SOFCs incorporating GDC interlayers fabricated under different processing conditions. (a–d) I–V and corresponding I–P curves measured between 650 and 800 °C for cells fabricated using pristine, Co_3O_4-assisted, CIP-assisted, and chemo-mechanical processing routes. (e–h)

Electrochemical impedance spectra collected under OCV conditions for the pristine, Co_3O_4-assisted, CIP-assisted, and chemo-mechanically processed cells, respectively.

3.3 Degradation Suppression through Chemo-Mechanically Stabilized Interfaces

Long-term galvanostatic durability testing was performed at 750 °C under a constant current density of 0.25 $A \cdot cm^{-2}$ for 460 h. This current density was selected as a practically relevant operating condition for long-term evaluation, while avoiding excessive concentration polarization and mass-transport limitations. It also represents a realistic operating load that can provide a favorable balance between power output and electrical efficiency for practical SOFC operation. As shown in Figure 3a, the cell maintained stable voltage output throughout the test. A minor voltage fluctuation near 325 h coincided with a brief workstation interruption and restart and did not alter the subsequent degradation trend. After an initial activation period during the first 200 h, the voltage decreased at 0.42 mV per 100 h during the subsequent 200–460 h period, corresponding to a normalized degradation rate of 0.48% per 1000 h relative to the voltage at 200 h. Higher-current durability testing remains necessary to further evaluate long-term performance under more demanding operating conditions. The observed degradation rate compares favorably with values reported for conventionally processed YSZ-based SOFCs employing GDC interlayers and high-temperature co-fired architectures, where interfacial degradation and cation interdiffusion often lead to more pronounced performance decay during long-term operation [12,41].

EIS was used to identify the main contribution to the observed performance loss. As shown in Figure 3b, R_Ω increased by only approximately 0.015 $\Omega \cdot cm^2$, from 0.082 to 0.097 $\Omega \cdot cm^2$, during the 460 h test, indicating that the electrolyte/interlayer/cathode ionic transport path remained largely stable. At LSCF/YSZ interfaces, Sr segregation and cation interdiffusion can promote the formation of ion-blocking phases such as $SrZrO_3$, which may increase the ohmic resistance [8,10,12]. The limited change in R_Ω therefore suggests that no substantial increase in interfacial ohmic resistance occurred during operation.

In comparison, R_p increased from 0.468 to 0.832 Ω·cm^2 over the same period. The DRT spectra in Figure 3c show that the high-frequency response remained relatively stable, while only minor changes occurred in the low-frequency region associated with gas transport. The most pronounced evolution occurred at intermediate frequencies, where the relaxation intensity increased progressively with aging. These features are commonly associated with electrode reaction processes, including surface exchange and charge transfer at electrochemically active interfaces and triple-phase boundaries [42,43]. The impedance evolution therefore points to a gradual deterioration in electrode kinetics rather than a substantial increase in gas-transport losses.

Post-test SEM further supports this interpretation. Compared with the initial state, the anode functional layer exhibited changes in pore distribution and a more heterogeneous microstructure after operation (Figure S7,S8). Such changes can reduce the number or accessibility of active reaction sites and contribute to the increase in R_p. Taken together, the EIS, DRT, and microstructural results indicate that electrode evolution, particularly within the anode functional layer, contributed substantially to the observed polarization increase [44].

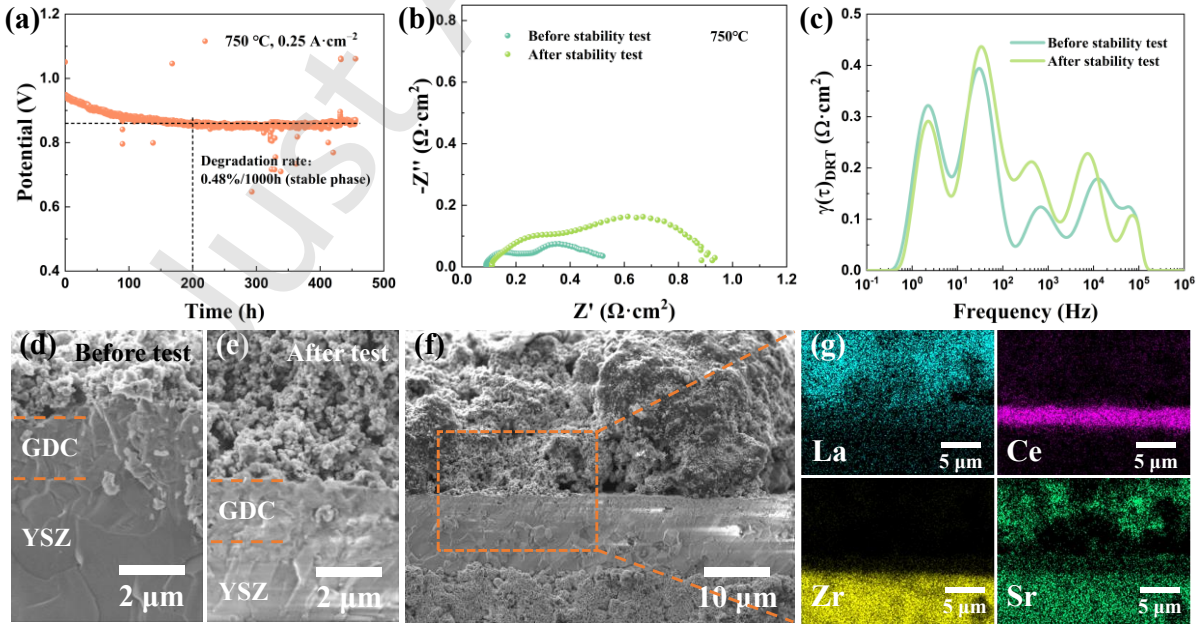

Figure 3 Long-term degradation behavior of the chemo-mechanically stabilized SOFC heterointerface. (a) Voltage evolution during galvanostatic operation at 750 °C under 0.25 A·cm^{-2}. (b) EIS spectra evolution during durability

testing, with EIS collected under OCV conditions. (c) DRT analysis derived from impedance spectra collected during aging, showing the progressive evolution of intermediate-frequency electrode processes. Cross-sectional SEM image of the SOFC (d) before and (e) after long-term operation at 750 °C. (f) Cross-sectional SEM image and (g) corresponding EDS elemental mappings of the electrolyte/cathode heterointerface after long-term operation, demonstrating suppressed interfacial reaction-layer formation.

Cross-sectional SEM and EDS mapping of the electrolyte/cathode interface are shown in Figure 3d,e and Figure 3f,g, respectively. The GDC interlayer remained dense and continuous after the 460 h test, and no continuous Sr-rich reaction layer attributable to Sr–Zr interfacial reaction was resolved by SEM-EDS. Thus, under the present operating conditions, the increase in polarization resistance was associated primarily with electrode microstructural evolution, while no pronounced interfacial reaction was detected.

3.4 Interfacial Stability under Accelerated Thermal Aging

To further evaluate the stability of the electrolyte/cathode interface under accelerated conditions, symmetric cells were aged in air at 850 °C for 600 h. The symmetric-cell configuration excludes anode-related degradation and allows the cathode/interlayer/electrolyte interface to be evaluated separately. A GDC-free reference was tested under the same conditions for comparison. This comparison evaluates the overall protective effect of the GDC interlayer rather than independently separating the contributions of Co_3O_4-assisted sintering and CIP treatment. The comparative thermal-aging results support the enhanced stability provided by the low-temperature-densified GDC interlayer relative to the GDC-free interface, while systematic aging of the individual processing routes would be required to further resolve their respective contributions.

Figure 4a,b compares the EIS evolution of the chemo-mechanically processed and GDC-free symmetric cell during thermal exposure at 850 °C for 600 h. The GDC-containing cell showed only minor impedance changes throughout the 600 aging period, whereas the GDC-free reference exhibited a more pronounced increase in R_p. The evolution of R_Ω and R_p is summarized in Figure 4c. The initial R_Ω values were 0.54 and 0.53 $\Omega \cdot cm^2$ for the GDC-containing and GDC-free cells, respectively,

indicating no measurable ohmic penalty from the GDC interlayer. After 600 h, R_Ω increased to 0.61 $\Omega \cdot cm^2$ for both cells, suggesting that bulk electrolyte transport remained largely unaffected. In contrast, R_p remained nearly unchanged for the GDC-containing cell but increased continuously for the GDC-free reference. Because the symmetric-cell configuration excludes anode-related contributions, the different R_p evolution reflects the different stability of the cathode/interlayer/electrolyte interfaces.

The corresponding microstructural observations are shown in Figure 4d–g. In the GDC-free reference, localized Sr enrichment was observed near the YSZ interface together with a continuous interfacial region showing enhanced Sr and Zr signals, consistent with the formation of an interfacial reaction region. The weak Sr signal distributed across the YSZ region should be interpreted cautiously because the Sr L and Y L emission lines are close in energy and may not be fully resolved by conventional EDS [45]. The analysis therefore focuses on localized interfacial Sr enrichment and the continuous reaction region rather than the weak background signal.

In contrast, the GDC-containing interface remained dense and structurally intact after 600 h at 850 °C. No comparable localized Sr enrichment or continuous Sr-containing reaction layer was resolved at the GDC/YSZ interface within the spatial and compositional resolution of SEM-EDS. Extensive Ce–Zr interdiffusion was also not detected. These observations are consistent with the function of the dense GDC layer as a diffusion barrier between the Sr-containing cathode and the YSZ electrolyte, limiting direct interfacial reaction during thermal aging.

Overall, the accelerated-aging results demonstrate that the low-temperature-densified GDC interlayer maintained the structural and electrochemical integrity of the cathode/electrolyte interface under 850 °C exposure for 600 h (Figure 4h). The GDC-containing interface therefore showed better stability than the GDC-free reference under the accelerated aging conditions. The individual contributions of CIP and Co_3O_4-assisted sintering were not separated in this test.

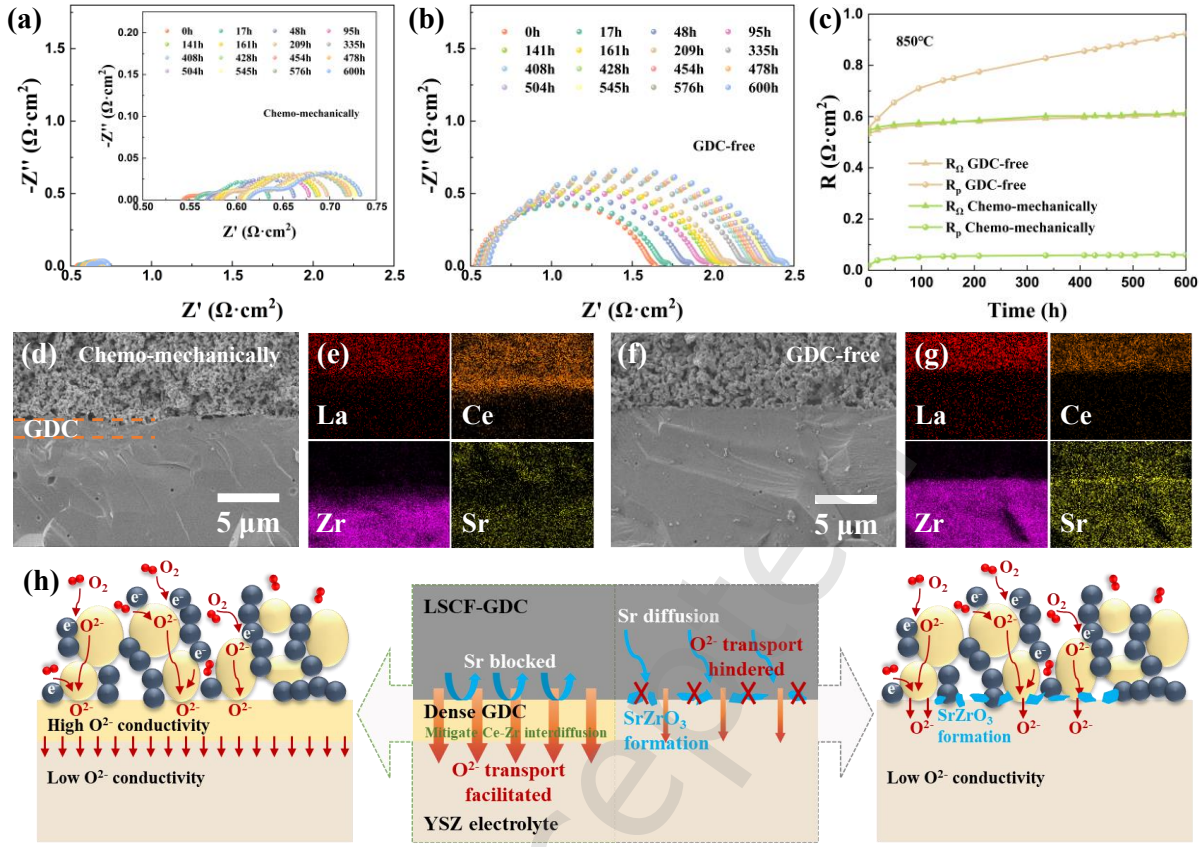

Figure 4 Accelerated thermal-aging behavior of chemo-mechanically stabilized SOFC heterointerfaces. (a,b) Time-dependent impedance spectra of chemo-mechanically processed and GDC-free symmetric cells during aging at 850 °C. (c) Evolution of R_Ω and R_p during 600 h thermal aging. Cross-sectional SEM images and corresponding EDS elemental mappings of (d,e) the chemo-mechanically stabilized heterointerface and (f,g) the GDC-free reference after aging. (h) Schematic illustration of the coupled chemical, electrochemical, and chemo-mechanical stabilization mechanisms enabled by the dense GDC interlayer.

3.5 Scale-Up of Chemo-Mechanically Regulated GDC Interlayers to Large-Area SOFCs

Practical deployment of SOFC technology requires that interfacial stabilization strategies remain effective at manufacturing-relevant scales. Scaling constrained ceramic films to large-area architectures introduces additional challenges (e.g., macroscopic stress accumulation, shrinkage heterogeneity, defect propagation) that become more severe with increasing lateral dimensions.

To evaluate the scalability of the proposed strategy, large-area SOFCs with dimensions of 10 × 10 cm^2 and an active area of 81 cm^2 were fabricated using the optimized chemo-mechanical process (Figure 5a,b). The successful fabrication of three large-area cells provides an initial assessment of

process feasibility and consistency, but is insufficient to establish large-area defect statistics or manufacturing reproducibility. Cross-sectional SEM observations of the large-area cell are shown in Figure 5c,d, where the position and approximate thickness (~1.8 μm) of the dense GDC interlayer are clearly identified. The GDC interlayer remained dense, continuous, and well adhered at the examined cross-sectional location, without any signs of macro-scale cracking or delamination. The observed cross-sectional microstructure suggests that the combined use of CIP and Co_3O_4-assisted sintering can help maintain interlayer continuity during large-area constrained densification.

The electrochemical performance of the large-area SOFCs was evaluated between 650 and 750 °C using hydrogen fuel and air (Figure 5e,f). Figure 5f compares the I–V characteristics of three independently fabricated 10 × 10 cm^2 cells (Cells 1–3) with an active area of 81 cm^2 at 750 °C. Cells 1 and 2 were measured from OCV down to 0.8 V to minimize additional high-load exposure and potential irreversible degradation, whereas Cell 3 underwent a full I–V sweep and delivered a peak power output of 60.6 W, corresponding to 0.75 $W \cdot cm^{-2}$. Because only Cell 3 was subjected to the full I–V sweep, its peak power output was not used for statistical comparison among the three cells. The power output at 0.8 V was therefore used as a common metric for comparison. Cells 1–3 delivered 42.0, 40.8, and 33.6 W at 0.8 V, respectively, corresponding to an average power of 38.8 ± 4.5 W. The optimized processing route was demonstrated on three independently fabricated cells, providing a preliminary assessment of process feasibility and consistency. However, the limited sample size does not establish suppression of microscopic defects at the large-area scale, and further batch-scale validation and large-area process-control studies are required. The lower area-specific performance of the large-area cells may arise from increased current-collection resistance, gas-distribution nonuniformity, temperature gradients, flow-field limitations, and the different LSCF–GDC composite cathode architecture used for scale-up [41,46].

The successful scale-up highlights the practical processing compatibility of the present strategy with large-area wet-processing routes. This contrasts with vacuum-based thin-film techniques (e.g., PLD

and ALD) that face practical limitations in size [15,17]. In contrast, the developed chemo-mechanical framework integrates with conventional, scalable processing routes, including screen printing, spin coating, and pressure-assisted compaction, without altering existing automated workflows.

The combined control of diffusion kinetics and green-state packing may also be applicable to other multilayer ceramic architectures in which constrained sintering and interfacial transport are closely coupled, including SOECs, oxygen transport membranes, and protonic ceramic electrochemical devices [47–49].

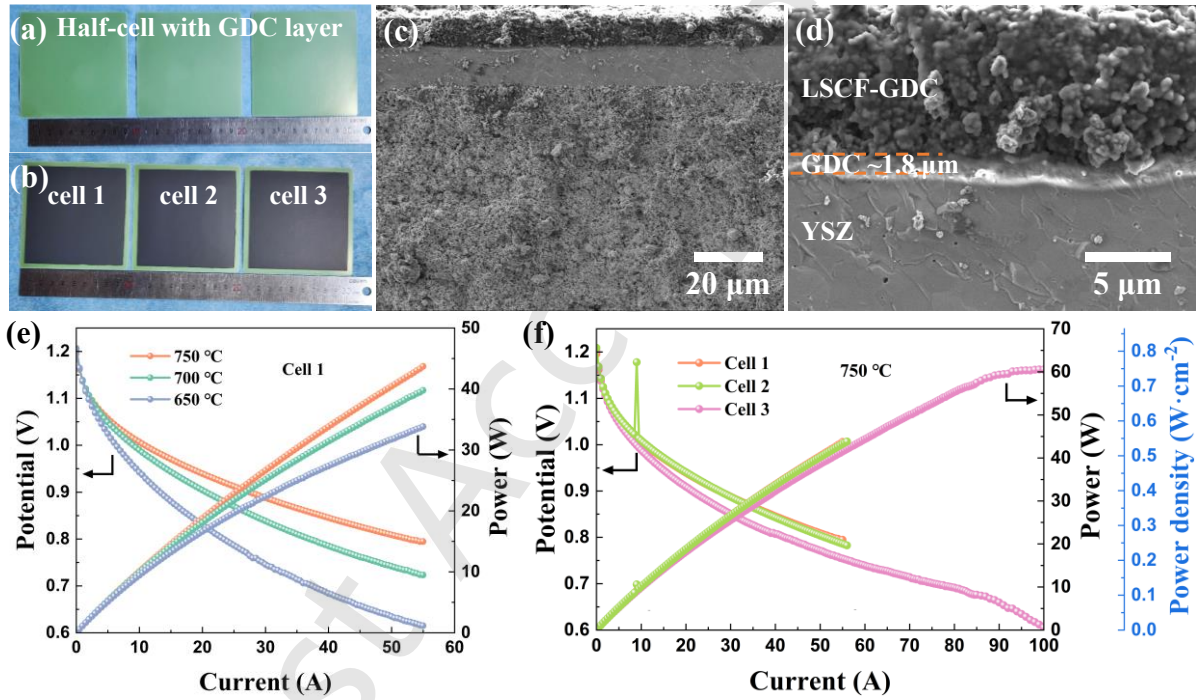

Figure 5 Scale-up of chemo-mechanically densified GDC interlayers to large-area SOFCs. (a,b) Photographs of the 10 × 10 cm^2 SOFC fabricated using the optimized chemo-mechanical densification strategy. (c,d) Cross-sectional SEM image of the large-area electrolyte/cathode heterointerface, showing preserved interlayer continuity after scale-up processing. (e) I–V and corresponding I–P characteristics of the large-area SOFC (Cell 1) measured at temperatures ranging from 650 to 750 °C. (f) I–V characteristics of three independently fabricated large-area SOFCs (Cells 1–3) at 750 °C. Cells 1 and 2 were evaluated from OCV down to 0.8 V, whereas Cell 3 underwent a full I–V sweep.

4 Conclusions

This work demonstrates that constrained densification of functional ceramic interlayers is strongly influenced by the interplay among pore evolution, mass transport kinetics, and constraint effects that develop during sintering. By integrating Co_3O_4-assisted sintering activation with CIP-enabled packing homogenization, we establish a chemo-mechanical regulation strategy that couples kinetic activation with green-state packing control to promote densification of constrained GDC films.

The synergistic regulation of transport kinetics and green-state microstructure enables near-complete densification of ultrathin GDC interlayers (98.5% apparent relative density) at 1200 °C, substantially lower than temperatures typically required for constrained ceria sintering. The dense and continuous GDC interlayer contributes to improved interfacial stability during both fabrication and operation, enabling sustained ionic transport and enhanced electrochemical durability.

The optimized cell achieves a peak power density of 1.36 $W \cdot cm^{-2}$ at 800 °C and maintains stable operation with an extrapolated degradation rate of 0.48% per 1000 h at 750 °C. Accelerated aging at 850 °C for 600 h further supported the enhanced stability of the engineered cathode/electrolyte interface relative to the GDC-free reference.

Overall, the combined use of Co_3O_4-assisted sintering and CIP provides a practical route to densify constrained GDC interlayers at 1200 °C while maintaining favorable electrochemical and interfacial characteristics. The large-area results further provide a preliminary demonstration that the process can be extended to 10 × 10 cm^2 cells, although additional batch-scale testing is required to establish manufacturing reproducibility.

Acknowledgements

The authors also gratefully acknowledge the financial support from the China Scholarship Council (CSC).

Funding

This work was supported by the program of Beijing Huairou Laboratory (No. ZD2022006A).

Author contributions

Fuhuan Wang: Methodology, Software, Writing – original draft. Fuhuan Wang, Yuechao Yao, Yucan Liu, Weifeng Zhang, Yanmin Wang, Xiaojie Cheng: Data curation, Validation. Jun Zhang, Yucun Zhou, Shaorong Wang, Hewu Wang: Conceptualization, Supervision, Writing – review and editing. Liangfei Xu, Minggao Ouyang, Jianqiu Li: Funding acquisition, Project administration.

Availability of data and materials

The data supporting the findings of this study are available within the article and its Supplementary Information. Additional data are available from the corresponding author upon reasonable request.

Competing interests

The authors have no competing interests to declare that are relevant to the content of this article.

Electronic Supplementary Material (ESM)

Supplementary figures, tables, experimental details, and additional electrochemical characterization are available in the online version of this article.

References

[1] Wachsman ED, Lee KT. Lowering the temperature of solid oxide fuel cells. *Science* 2011, 334: 935–939.

[2] Li T, Yang Y, Yang F, et al. High-oxygen vacancy cerium catalysts with NiFe alloy heterostructures: A pathway for efficient and stable biomass ethanol fuel tubular solid oxide fuel cells. *J Adv Ceram* 2025, 14: 9221143.

[3] Wang Y, Shi J, Gu X, et al. Toward mobility of solid oxide fuel cells. *Prog Energy Combust Sci* 2024, 102: 101141.

[4] Brett DJL, Atkinson A, Brandon NP, et al. Intermediate temperature solid oxide fuel cells. *Chem Soc Rev* 2008, 37: 1568–1578.

[5] Khan MZ, Mehran T, Song RH, et al. Controlling cation migration and inter-diffusion across cathode/interlayer/electrolyte interfaces of solid oxide fuel cells: A review. *Ceram Int* 2021, 47: 5839–5869.

[6] Lyu Q, Zhu T, Li Z, et al. Enhancement of the cathode/electrolyte interface by a sintering-active barrier layer for solid oxide fuel cells. *Int J Hydrogen Energy* 2023, 48: 15238–15247.

[7] Jiang SP. Development of lanthanum strontium cobalt ferrite perovskite electrodes for solid oxide fuel cells. *Int J Hydrogen Energy* 2021, 46: 26587–26614.

[8] Dang X, Lu Y, Fan Z, et al. Strategies to mitigate Sr segregation of the LSCF oxygen electrode for solid oxide cells. *J Mater Chem A* 2025, 13: 20268–20288.

[9] Kim J, Shim JH, Kim Y, et al. Activation of LSCF–YSZ interface by cobalt migration during electrolysis operation in solid oxide electrolysis cells. *Int J Hydrogen Energy* 2022, 47: 38114–38123.

[10] Monaco F, Ferreira-Sanchez D, Hubert M, et al. Oxygen electrode degradation in solid oxide cells operating in electrolysis and fuel cell modes: LSCF destabilization and interdiffusion at the electrode/electrolyte interface. *Int J Hydrogen Energy* 2021, 46: 31533–31549.

[11] Duan X, Wang H, Tade MO, et al. A review on solid oxide fuel cell durability: Latest progress, mechanisms and study tools. *Renew Sustain Energy Rev* 2022, 161: 112339.

[12] Yoshida H, Hattori M, Kishimoto H, et al. Interfacial evolution and long-term degradation behavior of LSCF/GDC/YSZ oxygen electrodes. *J Power Sources* 2020, 453: 227894.

[13] Wu S, Yan W, Ni N, et al. Densification of ceria-based barrier layer for solid oxide cells at lower sintering temperatures: A review. *J Adv Ceram* 2025, 14: 9221001.

[14] Xu Y, Farandos N, Rosa M, et al. Continuous hydrothermal flow synthesis of Gd-doped CeO_2 nanoparticles for inkjet printing of SOFC electrolytes. *J Eur Ceram Soc* 2019, 39: 4264–4272.

[15] Yang H, Lee H, Lim Y, et al. Atomic layer deposition of GDC cathodic functional thin films for oxide ion incorporation enhancement. *J Am Ceram Soc* 2020, 104: 86–95.

[16] Nurk G, Vestli M, Möller P, et al. Mobility of Sr in gadolinia-doped ceria barrier layers prepared using spray pyrolysis, pulsed laser deposition and magnetron sputtering methods. *J Electrochem Soc* 2016, 163: F88–F96.

[17] Jang SD, Jang SC, Lee H, et al. High-performing gadolinium-doped ceria interlayer for thin-film solid oxide fuel cells via sputtering process parameter control. *J Power Sources* 2025, 640: 236710.

[18] Zhu Z, Gong Z, Qu P, et al. Additive manufacturing of thin electrolyte layers via inkjet printing of highly-stable ceramic inks. *J Adv Ceram* 2021, 10: 279–290.

[19] Hanantyo MPG, Park J, Namgung Y, et al. Enhanced densification of screen-printed GDC interlayers for solid oxide fuel cells using nitrate-based precursor in various chelating agents as pore-filling solution. *Int J Hydrogen Energy* 2024, 88: 760–770.

[20] Ding C, Iwai H, Kishimoto M. Fabrication and characterization of YSZ/GDC bilayer electrolyte thin films by spray-coating and co-sintering. *ECS Trans* 2019, 91: 1139–1148.

[21] Wang F, Zhang W, Cheng X, et al. Scalable and facile fabrication of a dense $Ce_{0.9}Gd_{0.1}O_{2-\delta}$ buffer layer for solid oxide fuel cells. *Ceram Int* 2025, 51: 52606–52614.

[22] Bordia RK, Raj R. Sintering behavior of ceramic films constrained by a rigid substrate. *J Am Ceram Soc* 1985, 68: 287–292.

[23] Lee HW, Park M, Hong J, et al. Constrained sintering in fabrication of solid oxide fuel cells. *Materials* 2016, 9: 675.

[24] Green DJ, Guillon O, Rödel J. Constrained sintering: A delicate balance of scales. *J Eur Ceram Soc* 2008, 28: 1451–1466.

[25] Guillon O, Rödel J. Predicting sintering deformation of ceramic film constrained by rigid substrate using anisotropic constitutive law. *Acta Mater* 2010, 58: 5980–5988.

[26] Wang G, Jia C, Sun Z, et al. In situ densification of gadolinium-doped ceria interlayer by infiltration process in SOFC. *ECS Trans* 2019, 91: 1149–1156.

[27] Bjørk R, Frandsen HL, Pryds N. Modeling the microstructural evolution during constrained sintering. *Comput Mater Sci* 2016, 119: 114–122.

[28] Machado M, da Silva AL, Moraes LPR, et al. Interface segregation of iron sintering aid in gadolinium-doped ceria. *CrystEngComm* 2023, 25: 6102–6110.

[29] Nicholas JD, Mandowara S, Yang Q, et al. Effect of sintering aids on the stress evolution of constrained sintered gadolinium-doped ceria films. *ECS Trans* 2012, 45: 481–490.

[30] Murutoğlu M, Ucun T, Ulasan O, et al. Cold sintering-assisted densification of GDC electrolytes for SOFC applications. *Int J Hydrogen Energy* 2022, 47: 19772–19779.

[31] Kabir A, Espineira-Cachaza M, Fiordaliso EM, et al. Effect of cold sintering process (CSP) on the electro-chemo-mechanical properties of Gd-doped ceria (GDC). *J Eur Ceram Soc* 2020, 40: 5612–5618.

[32] Sim SM. Preparation of $Ce_{0.8}Gd_{0.2}O_{1.9}$ powder using CeO_2 powder and Gd precipitation and effect of CoO doping on sintering. *J Korean Ceram Soc* 2015, 52: 521–526.

[33] Mostafavi E, Babaei A, Ataie A. $La_{0.6}Sr_{0.4}Co_{0.2}Fe_{0.8}O_3$ perovskite cathode for intermediate temperature solid oxide fuel cells: A comparative study. *Iran J Hydrogen Fuel Cell* 2015, 4: 239–246.

[34] Li N, Verma A, Singh P, et al. Characterization of $La_{0.58}Sr_{0.4}Co_{0.2}Fe_{0.8}O_{3-\delta}$–$Ce_{0.8}Gd_{0.2}O_2$ composite cathode for intermediate temperature solid oxide fuel cells. *Ceram Int* 2013, 39: 529–538.

[35] Barsoukov E, Macdonald JR. Impedance Spectroscopy: Theory, Experiment, and Applications, 3rd ed. Hoboken: Wiley, 2018.

[36] Ciucci M, Chen C. Analysis of electrochemical impedance spectroscopy data using the distribution of relaxation times: A Bayesian and hierarchical Bayesian approach. *Electrochim Acta* 2015, 167: 439–454.

[37] Jud E, Huwiler CB, Gauckler LJ. Sintering analysis of undoped and cobalt oxide doped ceria solid solutions. *J Am Ceram Soc* 2005, 88: 3013–3019.

[38] Balice L, Dash A, Melcher C, et al. Constrained flash sintering of gadolinium-doped ceria thin layers. *J Am Ceram Soc* 2025, 108: e70033.

[39] Baral AK, Dasari HP, Kim BK, et al. Effect of sintering aid (CoO) on transport properties of nanocrystalline Gd doped ceria (GDC) materials prepared by co-precipitation method. *J Alloys Compd* 2013, 575: 455–460.

[40] Tsoga A, Naoumidis A, Nikolopoulos P. Interaction between YSZ and GDC in SOFC electrochemical cells. *Acta Mater* 2000, 48: 4709–4714.

[41] Lee JH, Lee SB, Kim BK, et al. Durability improvement of large-area anode-supported solid oxide fuel cell fabricated by four-layer sequential co-lamination and co-firing process. *J Power Sources* 2023, 573: 233160.

[42] Leonide A, Sonn V, Weber A, et al. Evaluation and modeling of the cell resistance and electrochemical performance of anode-supported solid oxide fuel cells. *J Electrochem Soc* 2008, 155: B36–B41.

[43] Kullmann L, Weber A, Ivers-Tiffée E. DRT analysis and transmission line modeling of ceria-based electrodes for solid oxide cells. *J Power Sources* 2023, 587: 233706.

[44] Yang W, Pan Z, Jiao Z, et al. Advanced microstructure characterization and microstructural evolution of porous cermet electrodes in solid oxide cells: A comprehensive review. *Energy Reviews* 2025, 4: 100104.

[45] Newbury DE, Ritchie NWM. Performing elemental microanalysis with high accuracy and precision by scanning electron microscopy/silicon drift detector energy-dispersive X-ray spectrometry (SEM/SDD-EDS). *J Mater Sci* 2015, 50: 493–518.

[46] Yokokawa H, Tu H, Iwanschitz B, et al. Fundamental mechanisms limiting solid oxide fuel cell durability. *J Power Sources* 2008, 182: 400–412.

[47] Hauch A, Ebbesen SD, Jensen SH, et al. Highly efficient high-temperature electrolysis. *J Mater Chem* 2008, 18: 2331–2340.

[48] Ebbesen SD, Jensen SH, Hauch A, et al. High temperature electrolysis in alkaline cells, solid proton conducting cells, and solid oxide cells. *Chem Rev* 2014, 114: 10697–10734.

[49] Wang Y, Ling Y, Wang B, et al. A review of progress in proton ceramic electrochemical cells: Material and structural design, coupled with value-added chemical production. *Energy Environ Sci* 2023, 16: 5721–5770.